Research Article | Vol. 10, No. 4 | 1 Apr 2019 | BIOMEDICAL OPTICS EXPRESS 1760
Biomedical Optics EXPRESS

Finger-mounted quantitative micro-elastography

ROWAN W. SANDERSON,[1,2,*] ANDREA CURATOLO,[1,2,3] PHILIP WIJESINGHE,[1,2,4] LIXIN CHIN,[1,2] AND BRENDAN F. KENNEDY[1,2]

[1]*BRITElab, Harry Perkins Institute of Medical Research, QEII Medical Centre, Nedlands and Centre for Medical Research, The University of Western Australia, Perth, Western Australia, 6009, Australia*
[2]*Department of Electrical, Electronic & Computer Engineering, School of Engineering, The University of Western Australia, 35 Stirling Highway, Perth, Western Australia, 6009, Australia*
[3]*Current address: Visual Optics and Biophotonics Group, Instituto de Óptica "Daza de Valdés", Consejo Superior de Investigaciones Cientificas (IO, CSIC), C/Serrano, 121, Madrid 28006, Spain*
[4]*Current address: SUPA, School of Physics and Astronomy, University of St. Andrews, KY16 9SS, UK*
**rowan.sanderson@research.uwa.edu.au*

Abstract: We present a finger-mounted quantitative micro-elastography (QME) probe, capable of measuring the elasticity of biological tissue in a format that avails of the dexterity of the human finger. Finger-mounted QME represents the first demonstration of a wearable elastography probe. The approach realizes optical coherence tomography-based elastography by focusing the optical beam into the sample via a single-mode fiber that is fused to a length of graded-index fiber. The fiber is rigidly affixed to a 3D-printed thimble that is mounted on the finger. Analogous to manual palpation, the probe compresses the tissue through the force exerted by the finger. The resulting deformation is measured using optical coherence tomography. Elasticity is estimated as the ratio of local stress at the sample surface, measured using a compliant layer, to the local strain in the sample. We describe the probe fabrication method and the signal processing developed to achieve accurate elasticity measurements in the presence of motion artifact. We demonstrate the probe's performance in motion-mode scans performed on homogeneous, bi-layer and inclusion phantoms and its ability to measure a thermally-induced increase in elasticity in *ex vivo* muscle tissue. In addition, we demonstrate the ability to acquire 2D images with the finger-mounted probe where lateral scanning is achieved by swiping the probe across the sample surface.

1. Introduction

For centuries, physicians have relied on the sense of touch to qualitatively assess disease based on changes in the mechanical properties of tissue, i.e., manual palpation [1]. The sustained and widespread clinical use of manual palpation is largely attributed to the dexterity of hand motion and its ease of use [2,3]. However, the inherent subjectivity, lack of quantification and relatively low spatial resolution, limit the efficacy of manual palpation in correctly identifying diseased tissue [4]. One proposed solution is elastography, a family of imaging techniques developed over the past 30 years that map tissue elasticity by combining medical imaging with mechanical deformation [5]. Elastography was initially developed using ultrasound [6,7] and magnetic resonance imaging [8], and has been proposed for a range of clinical applications, particularly in hepatology [9,10] and oncology [11]. More recently, optical coherence tomography (OCT)-based elastography, optical coherence elastography (OCE), has been developed to improve both the spatial resolution (to 10s–100s μm) and sensitivity (to nanometer-scale deformations) in comparison to other approaches, albeit to a relatively shallow imaging depth of ~1 mm in turbid tissue [12–18]. OCE is undergoing development in a range of fields, most prominently in ophthalmology [19], cardiology [20], and oncology [21,22]. As a photonics-based technique, OCE is amenable to

#351772 https://doi.org/10.1364/BOE.10.001760
Journal © 2019 Received 14 Nov 2018; revised 17 Jan 2019; accepted 5 Feb 2019; published 11 Mar 2019

Biomedical Optics EXPRESS

miniaturization into small form factor probes, such as needles and endoscopes [23–25]. Such probes have the potential to enhance the clinical applicability of OCE. Initially, OCE probes, such as needle OCE, were limited to measurements of strain, yielding qualitative assessments and providing low contrast in some instances [26]. For clinical applications, quantitative imaging can aid in the identification of diseased tissue, facilitate rapid interpretation of results and also enable more ready comparison of results obtained from different patients. More recently, to address this, there have been several demonstrations of quantitative OCE probes [25,27], however, in these demonstrations mechanical loading was applied using bulky mounted set-ups or by motorized stages that are impractical for routine use by clinicians.

Here, we propose a novel OCE probe, in which the sample arm of an OCE system is encased in a 3D-printed thimble and worn on the finger. This technique represents the first finger-mounted, and indeed wearable, version of OCE. In addition, more broadly, there have been few demonstrations of a free-hand OCE probe without the need for supporting apparatus [28]. Our methodology is based on quantitative micro-elastography (QME) [29,30], a compression-based OCE technique that utilizes phase-sensitive detection to estimate the elasticity of a sample by combining the surface stress, measured using a compliant layer, with the local axial strain measured throughout the OCT field-of-view. To realize finger-mounted QME, we extend on QME signal processing to generate accurate elasticity measurements in the presence of motion artifact induced by the finger.

Finger-mounted QME has the potential to preserve much of the dexterity and ease of use of manual palpation, whilst also providing the quantification, relatively high spatial resolution and depth-sectioning capability of OCE. This technique may increase the clinical applicability of OCE, particularly in scenarios where the use of a relatively bulky handheld probe is not convenient, e.g., in assessing if residual tumor is present in small cavities following excision of the main tumor mass in breast-conserving surgery. In this paper, we provide experimental validation of finger-mounted QME on homogeneous, bi-layer and inclusion phantoms and *ex vivo* muscle tissue. We demonstrate that finger-mounted QME is capable of measuring the elasticity of silicone phantoms to within 21% of the expected value (compared to 8% for a bench-top implementation of QME [29]), and that it can distinguish the change in mechanical properties between raw and cooked kangaroo muscle tissue. Furthermore, we demonstrate a method to perform 2D scanning in finger-mounted QME by swiping the probe across the sample surface with a gentle, yet increasing, compression. The results presented in this paper highlight the potential of finger-mounted QME for development towards clinical applications that currently rely on manual palpation.

2. Methods and materials

2.1 Probe design

Finger-mounted QME comprises a fiber probe (illustrated in Figs. 1(a) and 1(b)) connected to a spectral-domain OCT system (TEL320, Thorlabs, USA) with a central wavelength of 1300 nm, a 3 dB-bandwidth of 170 nm, and a measured full-width-at-half-maximum (FWHM) axial resolution of 5.2 μm. The probe is configured as a common-path interferometer to maximize displacement sensitivity [10], which was measured to be 1.44 nm for an OCT signal-to-noise (SNR) of 40 dB [30]. The probe consists of a single mode fiber (SMF) spliced to a 270 μm length of graded-index (GRIN) fiber (Miniprobes, Australia) that focuses the beam into the sample. The fiber probe is embedded within a thin channel along the underside of a 3D-printed thimble, as illustrated in Fig. 1(b), using an ultra-violet-curable optical adhesive (NOA68, Norland Products, USA). The adhesive also seals the fiber in place at the tip of the thimble (adhesive thickness, 70 μm) and provides the reference reflection in the common-path interferometer. In finger-mounted QME, A-scans are acquired at 10 kHz.

Two fiber probes were used in this study, manufactured to the same specifications; Probe 1 was used to generate the results presented in Figs. 2-4, and Probe 2 was used for Figs. 1, 5-7. The working distance of Probe 1 was 1.9 mm from the tip of the probe and the FWHM

Biomedical Optics EXPRESS

lateral resolution at the focus was measured to be 17.6 µm, whilst Probe 2 had a working distance of 1.6 mm and a measured FWHM lateral resolution at the focus of 12.5 µm. The usable imaging depth for these probes was ~800 µm, therefore the beam properties had minimal effect on the lateral resolution with depth. A beam profile of Probe 2 in both *x*- and *y*-directions is presented in Fig. 1(c). The beam profile was taken in the plane orthogonal to the direction of the beam and the FWHM *x*- and *y*-diameters were measured along the major and minor beam axes, demonstrating a profile that closely resembles that of an equivalent ideal Gaussian beam. A small deviation from the ideal Gaussian beam profile can be observed in this figure. This is likely due to aberrations caused by the cured optical adhesive at the fiber tip.

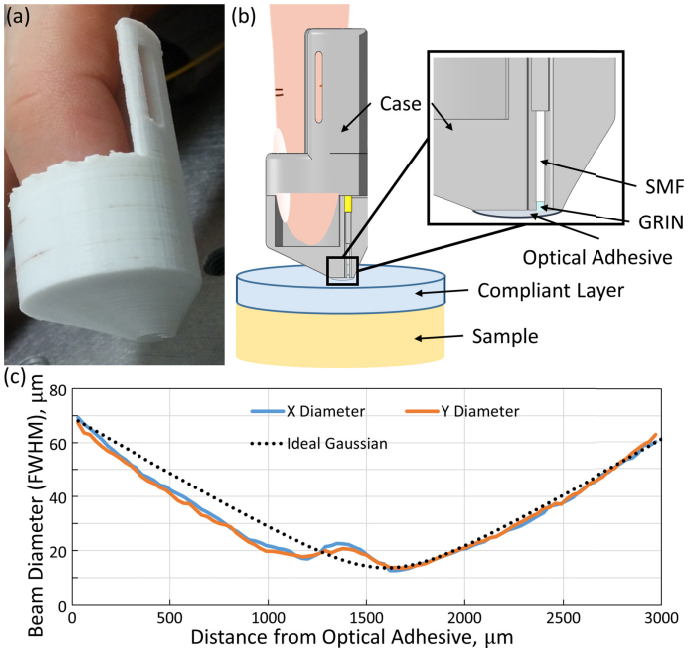

Fig. 1. Finger-mounted QME probe (a) photograph, (b) schematic with inset showing the fiber probe and optical adhesive. (c) Beam profile of Probe 2 compared to an ideal Gaussian beam.

2.2 Phantom and compliant layer fabrication

Five cylindrical, homogeneous tissue-mimicking silicone phantoms, each with a radius and thickness of 5 mm and 2 mm were used as test targets to assess the probe's accuracy in measuring elasticity. The phantoms were fabricated by mixing a room-temperature-vulcanizing silicone elastomer and curing agent together in addition to a non-crosslinking polydimethylsiloxane (PDMS) oil (Wacker, Germany) [31]. The mechanical properties of the phantoms were controlled by varying the elastomer type and mixing ratios. To generate optical scattering, 2 $mg.ml^{-1}$ of titanium dioxide (TiO_2) powder (Sigma Aldrich, product 232033) was added to the phantoms. The phantoms were fabricated to have elastic moduli in a range found in soft tissues (6.5–160 kPa, measured at 10% absolute strain) and were characterized using a uniaxial compression device, which we considered to be the 'gold standard' for characterization of mechanical properties. Hereon, we refer to the elastic moduli measured by the compression device as 'expected'. The measured and expected results of one such phantom are plotted against stress, rather than the conventional strain, in Fig. 2(e), for consistency with the general case of a sample of unknown thickness, where the absolute strain is unknown. In addition to homogeneous phantoms, a bi-layer phantom was fabricated, with the distance from the nearest surface of the phantom to the boundary between the layers

Biomedical Optics EXPRESS

located within the OCT field of view, allowing us to conveniently assess the probe's ability to detect boundaries within samples. The top/bottom layers had elastic moduli of 24 kPa/160 kPa, contained 0.5 $mg.ml^{-1}$ /3 $mg.ml^{-1}$ of TiO_2, and were 0.4 mm/3 mm thick, respectively. An inclusion phantom was also fabricated for the 2D scans. In this phantom, a stiff inclusion was embedded within a softer bulk material. The elastic modulus of the bulk was 24 kPa and of the inclusion was 160 kPa, both measured at 10% strain. Optical contrast was provided by adding 0.5 $mg.ml^{-1}$ to the bulk and 3 $mg.ml^{-1}$ of TiO_2 to the inclusion. The inclusion had dimensions (length × height) of ~1 mm and ~0.5 mm, respectively. The compliant layers used to estimate stress in QME were also fabricated from this silicone. In the homogeneous scans, the compliant layer material matched that of the sample and for the bi-layer and 2D scans, the compliant layers had an elastic modulus of 24 kPa at 10% strain. The compliant layers were all ~500 µm thick and contained no scatterers to ensure that the OCT SNR in the sample was maximized.

2.3 Finger-mounted QME measurements

Finger-mounted QME is based on a technique previously implemented in a bench-top imaging system [29]. In this approach, phase-sensitive detection is used to measure both the stress at the sample surface and the depth-dependent strain in the sample and elasticity is quantified as the ratio of these parameters [29]. To measure stress, a compliant layer is placed on the surface of the sample. The layer is nonlinear-elastic, displaying an increasing effective elastic modulus with strain [29]. Using the known stress-strain characteristic of the layer, measuring the strain in the layer using OCT allows us to calculate the axial stress at the layer-sample interface [32]. The strain in the sample was measured from OCT data as the slope of axial displacement using a finite difference approach [33].

The probe is worn on the finger and is forward-facing, such that the light is incident orthogonally to the tissue surface, assuming that the finger is positioned perpendicular to the sample surface. To deform the sample, axial compression is applied by the finger to both the compliant layer and the sample. A-scans are acquired and assembled to form a motion-mode (M-mode) image, as shown in Fig. 2(a). Figure 2(b) shows the axial displacement, u_z (estimated from the phase difference, $\Delta\varphi$) between consecutive A-scans, according to, $u_z = \Delta\varphi\lambda/4\pi n$, where λ is the central wavelength of the OCT light source and n is the material's refractive index [34].

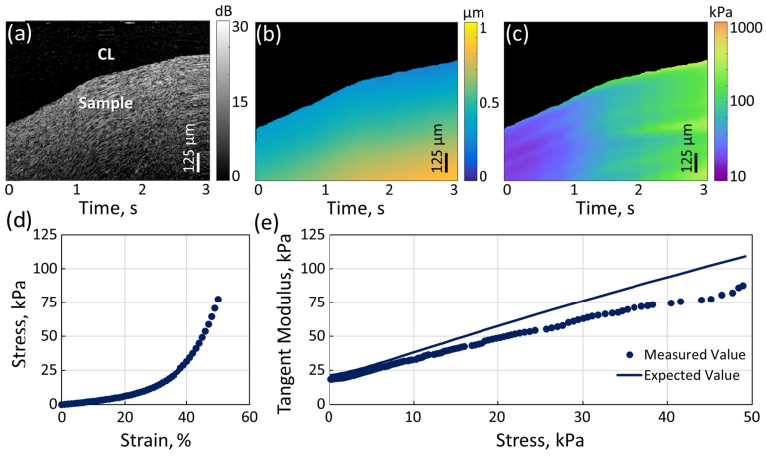

Fig. 2. (a) OCT M-mode, (b) axial displacement, and (c) tangent modulus maps plotted over time. In (b) and (c), the compliant layer (CL) is masked in black. (d) Stress-strain curve of the compliant layer material and (e) tangent modulus plot measured with increasing stress in a phantom, evaluated from tangent modulus map shown in (c).

Biomedical Optics EXPRESS

Key to the reconstruction of elasticity from finger-mounted QME data is the implementation of a number of filtering steps. The filtering performed on the displacement to reduce the effect of motion artifact is described in the following paragraph and is illustrated in Fig. 3. The layer-sample interface was determined for every A-scan using Canny-based edge detection [29]. Starting with the first A-scan, the axial displacement in the range 300–324 µm below this interface was cumulatively summed for every consecutive A-scan, until a threshold of 350 nm was reached. Analyzing the axial displacement over this depth helped to reduce the impact of surface friction on the displacement whilst remaining in a region of high OCT SNR. If 350 nm was reached too quickly (<3 A-scans) or too slowly (>40 A-scans), the displacement data was assumed to be noisy, and the initial A-scan was discarded. This was repeated for all A-scans. 350 nm was empirically selected for the threshold as it allowed us to obtain a strong signal well above the displacement noise floor and prevent significant decorrelation effects. A block diagram describing the signal processing is shown in Fig. 3(a). In the M-mode image in Fig. 3(b), discarded A-scans are represented by vertical, cyan lines. Figure 3(c) displays the filtered OCT image after the selected A-scans had been discarded and the remaining A-scans had been stitched together. After filtering, the displacement map was smoothed with a Gaussian filter (σ_{depth} = 12 µm and σ_{time} = 15 ms), and then sub-sampled every one-hundredth A-scan (one every 10 ms), in order to increase processing speed without noticeable degradation in image quality (Fig. 2(b)). A second Gaussian filter was applied on the sub-sampled displacement to further reduce noise in the strain calculation (σ_{depth} = 24 µm and σ_{time} = 300 ms). Strain was estimated as the gradient of the axial displacement with depth using a finite-difference approach [33]. This is termed 'incremental strain' as it describes the strain induced between consecutive A-scans. This approach allowed us to accommodate for a variable range of compression applied by the finger which is of key importance in finger-mounted QME, given that the velocity of the finger is uncontrolled.

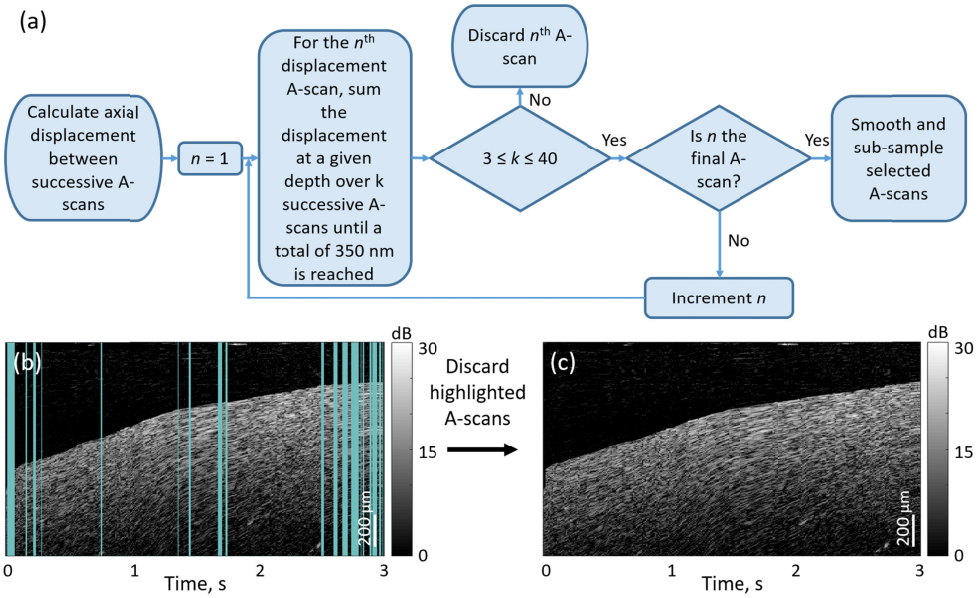

Fig. 3. (a) Block diagram representation of the filtering scheme used to reduce hand motion artifacts. (b) M-mode scan illustrating discarded A-scans in cyan. (c) The filtered OCT image.

The absolute strain in the layer was determined by measuring the thickness of the layer from the layer-sample interface in the OCT scan. Tangent modulus (the gradient of the stress over strain, equivalent to the Young's modulus in linear-elastic materials) in the layer is estimated from the absolute strain using the pre-calibrated stress-strain curve of the silicone, which is represented in Fig. 2(d) [29]. The axial incremental stress at the layer-sample

Biomedical Optics EXPRESS

interface is then calculated as the product of the layer modulus and the layer incremental strain. The tangent modulus of the sample is estimated by dividing the axial incremental stress in the layer by the incremental strain in the sample (Fig. 2(c)), under the assumption that the stress is constant with depth. Tangent modulus represents the effective modulus of a material at a particular strain and we subsequently refer to it as 'elasticity'. In Fig. 2(c), the measured elasticity increases with time. This is expected as the silicone phantom is a nonlinear elastic material. In Fig. 2(e), the elasticity measured both with the probe and the uniaxial compression device are plotted as a function of stress and close correspondence is demonstrated.

3. Results

3.1 Homogeneous silicone phantoms

Figure 4 shows a plot of the mean elasticity measured at 10% strain with the finger-mounted probe for five homogeneous silicone phantoms of varying elasticity against the expected elasticity (blue dots), measured using the uniaxial compression device. The red line indicates the ideal outcome where the measured elasticity is equal to the expected elasticity and the error bars represent one standard deviation across five separate measurements of each silicone sample. As the elasticity of each silicone sample is different, the corresponding stress at 10% strain varies in each case. The stresses of these samples were measured to be 0.5, 1.9, 4.6, 7.6 and 16 kPa respectively, when using the finger-mounted probe. The results show a strong correspondence between the measured and expected elasticity with a mean absolute percent error (MAPE) of 13%. The mean elasticity measured for each silicone sample is within 21% of the expected elasticity (compared to 8% for bench-top QME) [29]. The increased error using the finger-mounted probe is likely due to the variability of hand motion and an increase in friction, which is explained further in the Discussion.

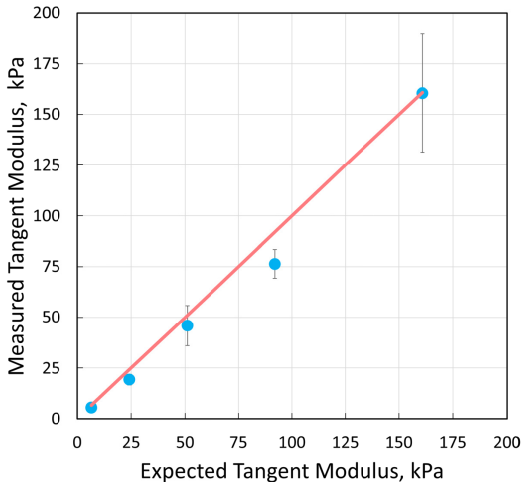

Fig. 4. Mean tangent moduli measured in five homogeneous phantoms of varying elasticity (blue dots) compared to expected values measured with uniaxial compression (red line). The error bars show one standard deviation.

3.2 Bi-layer silicone phantoms

In order to validate the ability to delineate two materials with varying mechanical properties in finger-mounted QME, measurements were performed on the bi-layer phantom. The M-mode OCT image is shown in Fig. 5(a). Figure 5(b) presents the corresponding OCT SNR, averaged over 50 A-scans, taken about the red line in Fig. 5(a). The individual layers can be distinguished by the change in signal intensity and attenuation. In Fig. 5(b), the boundary between the compliant layer and the top layer of the phantom is identified by the green

Biomedical Optics EXPRESS

diamond, whilst the yellow triangle indicates the boundary between the top (Layer 1) and bottom (Layer 2) layers of the phantom.

Figure 5(c) displays a map of the elasticity measured with the finger-mounted probe in the bi-layer phantom with the compliant layer masked out. In both layers, an increase in elasticity is observed with time. This is expected as the layer materials are nonlinear and therefore stiffen with increasing stress. The difference in elasticity between Layer 1 and Layer 2 is further illustrated in Fig. 5(d), which shows a plot of the elasticity over depth along the red line in Fig. 5(c), which corresponds to an applied stress of ~5 kPa. The boundary between layers measured using elasticity is consistent with the boundary determined from the corresponding OCT plot in Fig. 5(b). The elasticity in Layer 1 (between 400 and 600 µm) is noticeably lower than the elasticity in Layer 2 (beyond 600 µm in depth), as expected. The interface between the two layers is blurred because of the Gaussian smoothing applied to reduce noise. In Fig. 5(e), plots of the measured (dotted lines) and expected (solid lines) elasticity are presented over the applied stress from the corresponding regions of interests (ROI) shown in Fig. 5(c). The measured values in Fig. 5(e) are taken from the axially averaged elasticity within the ROI denoted by the blue (soft layer) and orange (stiff layer) dotted lines in Fig. 5(c). In this plot, close correspondence with the gold standard uniaxial compression device is observed.

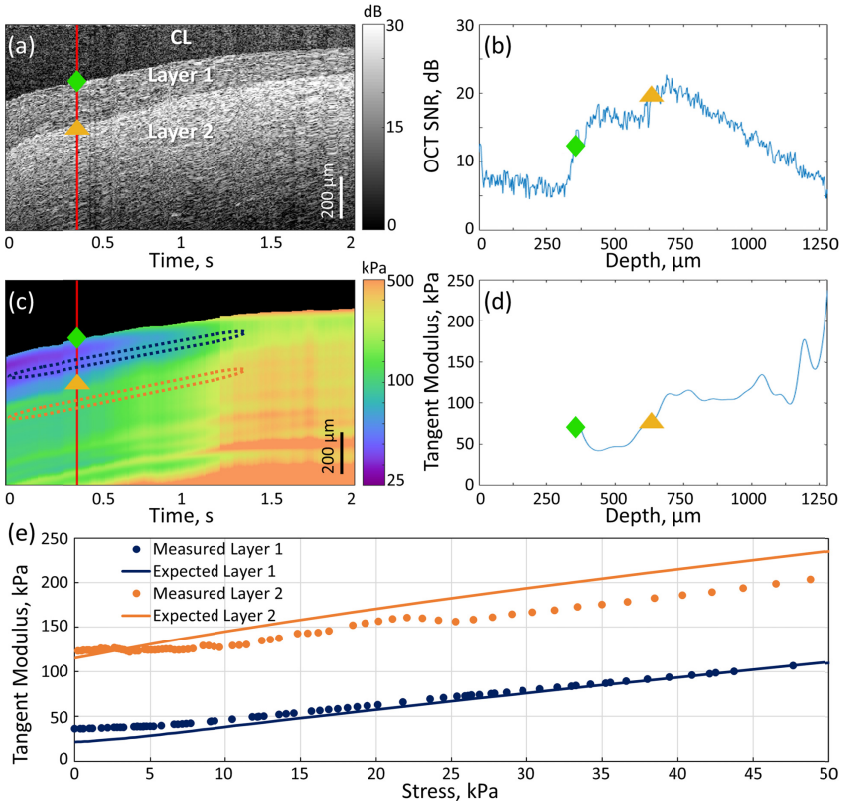

Fig. 5. Finger-mounted QME on a bi-layer phantom. (a) M-mode OCT image showing the compliant layer (CL), soft layer (Layer 1) and stiff layer (Layer 2) and (b) OCT SNR with depth averaged over 50 A-scans, where the green diamond indicates the upper layer boundary and the yellow triangle indicates the lower. (c) Corresponding elastogram with ROIs overlaid (CL masked in black) and (d) tangent modulus vs depth with diamond and triangles representing the same boundaries as in (b). Both (b) and (d) were taken over the A-scan corresponding with the red lines in (a) and (c). (e) Measured tangent moduli of Layer 1 (blue) and Layer 2 (orange) layers plotted on the same axes as the respective expected measurements, acquired through uniaxial compression.

Biomedical Optics EXPRESS

Compared to the compression test, the finger-mounted probe consistently overestimated the elasticity of Layer 1, but underestimated that of Layer 2, with a MAPE of 22% and 8%, respectively. Layer 2 exhibited increasing error with increasing stress. The cause of this error is explained further in the Discussion.

3.3 Kangaroo muscle

Finger-mounted QME was demonstrated on a 1 cm^3 excised section of kangaroo muscle tissue. Scanning was first performed on the raw tissue. After scanning, the sample was cooked in boiling water in a vacuum-sealed bag for four minutes and re-scanned. Figures 6(a) and 6(c) show M-mode OCT and QME images, respectively, of the raw sample. Similarly, Figs. 6(b) and 6(d) show M-mode OCT and QME images, respectively, of the sample after cooking. Comparing Fig. 6(a) to 6(b) reveals that cooking the tissue resulted in an increase in the OCT SNR, which may be caused by a reduction in water content [35]. Similarly, Figs. 6(c) and 6(d) display a marked increase in elasticity after cooking. Figure 6(e) highlights the variation in elasticity between the raw (blue) and the cooked (orange) samples as a function of stress, axially averaged over the regions indicated by the dotted blue and orange outlines in Figs. 6(c) and 6(d), respectively.

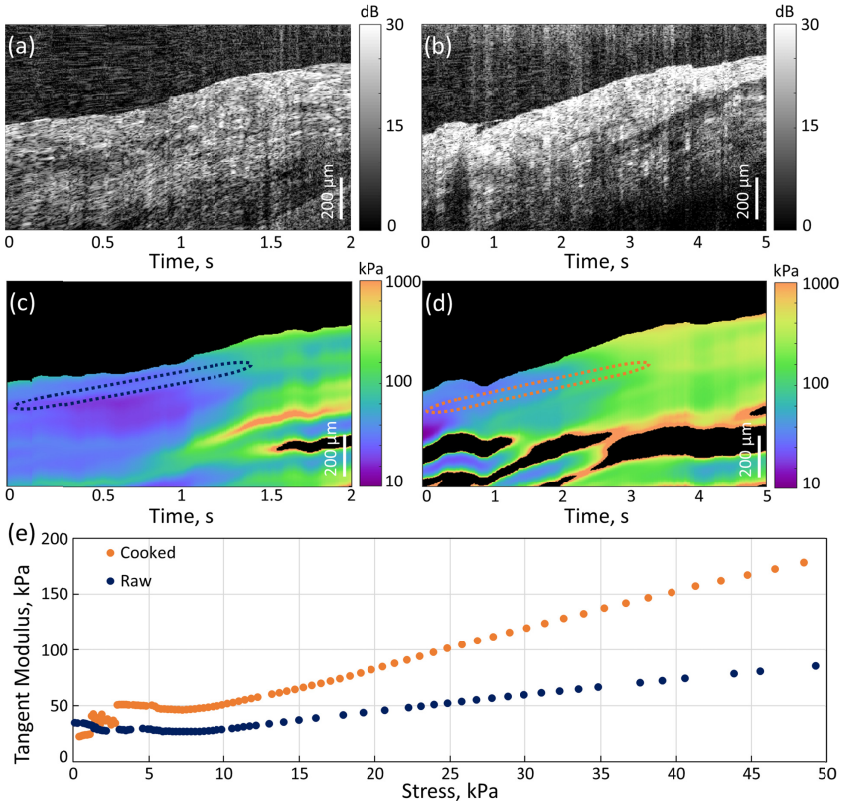

Fig. 6. OCT M-mode scans of (a) raw kangaroo muscle and (b) the same region of tissue after being cooked for four minutes. The elastograms of (c) the raw and (d) the cooked muscle with ROIs represented by dotted lines (CL masked in black). (e) Tangent modulus measurements for the ROIs in the cooked and raw sample.

It can be seen in Fig. 6(e) that the difference in elasticity between the raw and cooked samples becomes more prominent at higher stresses. For example, at a stress of 10 kPa, the elasticity of the raw and cooked tissue was 29 kPa and 50 kPa, respectively, compared to 117 kPa and 203 kPa at a stress of 50 kPa. This change in mechanical properties was

Biomedical Optics EXPRESS

confirmed qualitatively during the experiment by manual palpation and is consistent with prior studies on muscle tissue from other species [36]. We can see in Fig. 6(e) that the measurements for the cooked sample in the stress range 0-3 kPa, show a lower elasticity than the raw sample. This discrepancy is likely due to the probe not being positioned exactly perpendicular to the surface, decoupling the direction of the applied force and the axis which is scanned, resulting in a lower measured elasticity. This phenomenon is noticeable in tissue scans due to the heterogeneous structure, however, it reduces with higher stresses. This is most likely because of the operator's finger naturally tending towards perpendicular in order to apply higher forces to the sample [37].

3.4 2D scanning on a silicone inclusion phantom

In addition to M-mode scanning, as shown in Fig. 7, we also acquired preliminary 2D scans with finger-mounted QME by swiping the finger across a silicone inclusion phantom whilst acquiring A-scans. A compliant layer was placed on the inclusion phantom and the probe was brought into contact with the layer. During scanning, the finger applied both a lateral and axial motion, resulting in a ramp compression to the compliant layer and phantom. The increasing axial compression is a function of lateral position and ensured sufficient incremental strain was applied between consecutive A-scans. The speed at which the finger was swept across the sample was determined empirically by observing the real-time OCT image. The scans presented in Fig. 7 were taken on the inclusion phantom described in Section 2.2. The contrast between the surrounding bulk and the embedded inclusion is visible in the OCT image shown in Fig. 7(a). It is worth noting that the total length of the scan was ~5 mm and the inclusion was 1 mm wide. Considering this, it is apparent from Fig. 7 that the scanning performed by the finger is non-uniform, highlighting the effect of varying speeds of lateral hand motion. This results in a difference between the perceived and true dimensions of the imaged features, suggesting that a mechanism to compensate for this non-uniform scanning is required. This issue is described in more detail in the Discussion.

In finger-mounted QME, we consider compressive strain to be negative, and tensile strain to be positive [38]. Furthermore, we assume that compression is uniform and uniaxial. This, however, does not always hold true as mechanical heterogeneity and complex surface topologies can introduce tensile strain as well as compressive strain [38]. This is evident in 2D finger-mounted QME as the probe sweeps over the boundary between the bulk and inclusion, where regions of tensile strain were measured. To account for the presence of both compressive and tensile strain, Fig. 7(b) displays the magnitude of the elasticity, taken from both the positive (tensile) and negative (compressive) strains. The mean measured elasticity and standard deviation of this scan was 51 ± 4 kPa and 318 ± 67 kPa over 10–15% preload strain in the bulk and inclusion, respectively. These values are approximately twice the expected elasticity. While the contrast between the inclusion and bulk is apparent, there are regions of high elasticity that appear as orange lines in Fig. 7(b). The local boundary between tensile and compressive strain crosses zero, resulting in an asymptote in elasticity, corresponding to the orange lines. Due to the large smoothing kernels used in the processing code, this artifact also effects the surrounding regions of the bulk and inclusion, contributing to the overestimation of elasticity in these regions. This can be observed in the thin region of bulk above the inclusion. The mean measured elasticity in this region is 125 ± 12 kPa, ~2.5 times the measured elasticity in the rest of the bulk. Furthermore, the use of a logarithmic scale reduces the contrast of this particular region relative to the inclusion, however, there is still sufficient contrast in the elasticity measurements to delineate the inclusion from the bulk.

Biomedical Optics EXPRESS

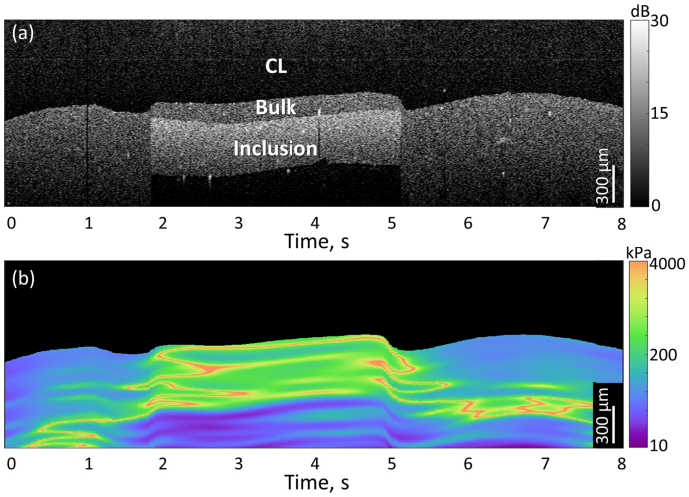

Fig. 7. (a) 2D-OCT scan over a stiff silicone inclusion embedded within a soft silicone bulk and (b) the corresponding 2D elasticity map with the *x*-axis given in seconds (CL masked in black).

Silicone, like tissue, exhibits a nonlinear stress-strain relationship, however, for small changes in strain, this relationship can be approximated as linear. In 2D scanning, we aim to limit the strain in the sample to 0–20% so that the measurements are taken from an approximately linear region of the stress-strain curve. This ensures that the elasticity measured in the bulk will be constant over the whole scan. Uniform elasticity in the surrounding bulk, allows 2D scanning to detect features of interest such as the inclusion shown in Fig. 7(b), based on mechanical contrast. This presents an additional problem, however, as the incremental strain is now reduced, which in turn leads to lower strain SNR in finger-mounted QME and a reduction in signal quality. Despite these issues, Fig. 7 presents high contrast between the inclusion and surrounding bulk in both the OCT image and elastogram, demonstrating the potential of 2D finger-mounted QME.

4. Discussion

In this paper, we have presented finger-mounted QME, a technique that provides quantitative measurements of the mechanical properties of soft tissue using a wearable elastography probe. While previous OCE probes such as needle-based OCE aim to replace manual palpation, finger-mounted QME offers the unique advantage of complementing manual palpation with OCE imaging. In needle OCE, as the needle tip is distal to the hand and because the needle is rigid, the dexterity of manual palpation is inherently lost. Using this probe, we have demonstrated the capability to measure elasticity in silicone phantoms and to delineate the mechanical properties of heterogeneous samples. Our approach utilizes a compact implementation of QME, which has potential for use in confined spaces such as surgical cavities, with the tradeoff of an additional 13% error compared to bench-top QME [29]. This represents a nominal increase in error as the mechanical contrast between healthy and diseased tissue is often significantly greater than this error. For example, invasive ductal carcinoma in breast tissue is up to seven times stiffer than adipose tissue [39], likewise, cirrhotic liver tissue is approximately twice as stiff as healthy liver tissue [40].

The error in the finger-mounted QME measurements is attributed largely to the frictional force between the compliant layer and the sample, which restricts lateral expansion of the compliant layer. As the silicone is incompressible, higher friction results in restricted deformation of the compliant layer for the same stress. Therefore, the absolute stress derived from the compliant layer is typically underestimated, leading to an underestimation of the elasticity of the sample [41], as can be seen in Fig. 2(e). In bench-top QME, PDMS oil is

Biomedical Optics EXPRESS

applied to both sides of the compliant layer to mitigate this friction on both the imaging window and the sample [29]. In finger-mounted QME, however, PDMS oil is only applied to the probe-compliant layer interface as PDMS oil between the sample and compliant layer, coupled with the indenter-like profile of the probe tip, will cause the compliant layer to slip during scanning. At higher stresses, the compliant layer will slip completely off the sample, therefore preventing the estimation of elasticity. Applying oil to only the probe-compliant layer interface, results in an increased error due to friction compared to the bench-top counterpart. This error is also seen in the measurement of Layer 2 for the bi-layer scans presented in Fig. 5, however, in the same scan Layer 1 was slightly overestimated. This overestimation may be due to a similar effect, where Layer 2 restricts the lateral expansion of the thinner top layer, resulting in a lower axial strain and a higher measured elasticity, which was prominent enough to dominate the effects of friction at the compliant layer-Layer 1 interface. Finger-mounted QME demonstrated a MAPE of 22% and 8% for the upper and lower layers respectively, which is similar to the 15% reported by benchtop QME [29]. This shows that despite the simplified optical design and hand-motion associated with the finger-mounted probe, this technique is still capable of reproducing elasticity measurements with high accuracy and providing high contrast between different materials.

One of the key challenges facing finger-mounted QME is the implementation of accurate 2D and, eventually, 3D scanning. In this paper, we have presented preliminary 2D scans that serve as an example for the extension of the technique to 2D. These results were acquired by swiping the finger along the tissue surface and using the finger motion as both the scanning and mechanical loading mechanism. A main issue with this approach is that the reconstruction of OCT images and elastograms does not account for non-uniform velocities of the scanning finger. Without implementing a method to accurately track the motion of the probe, it is challenging to determine the location of A-scans within a 2D scan, resulting in distortion of the apparent dimensions of sample features as seen in Fig. 7. This could be overcome by using a lateral scanning mechanism, such as compact microelectromechanical system (MEMS) scanning mirrors, already deployed in other OCT probes [42–45]. This, however, would add considerable bulk to the design, increasing the probe footprint and reducing dexterity. Alternatively, an external tracking system, such as a magnetic position sensor, could be used to determine the probe location during the scan [46]. However, the spatial and temporal resolution of magnetic tracking systems is low compared to OCT, and such a system would likely need to be complemented by additional sensors, such as accelerometers, or some form of image registration to infer the motion of the probe from the changes in the acquired images. Another option would be to exploit the decorrelation time of the speckle pattern to estimate velocity [47]. This approach has been employed to account for non-uniform rotation distortion (NURD) in endoscopic OCT applications [47], and could be modified to account for linear motion across the sample surface in finger-mounted QME.

Finger-mounted QME aims to improve diagnostic outcomes by complementing manual palpation with a quantitative assessment of disease. One area of potential application, is in breast-conserving surgery, which relies heavily on manual palpation to detect traces of tumor during surgery [4]. During this procedure, the surgeon strives to excise the tumor, in addition to a thin surrounding layer of healthy tissue [48,49]. Surgeons then often manually palpate the surgical cavity to determine if there is residual tumor in the patient [4]. However, in 20–30% of breast-conserving surgery patients, additional surgery is required as not all of the residual tumor was excised [50]. Finger-mounted QME scanning of the cavity walls could improve the detection of residual tumor. By looking for changes in the mechanical properties of cancerous tissue, our technique could potentially identify tumor that was not picked up by manual palpation. Finger-mounted QME also holds potential in applications relating to the intraoperative detection of hepatic metastases [51] and pancreatic insulinomas [52], both of which typically present as stiff lesions. As with BCS, surgeons performing these procedures rely on manual palpation to detect changes in the mechanical properties of tissue to guide

Biomedical Optics EXPRESS

them in locating the malignancies and finger-mounted QME has the potential to improve on this existing approach [51,52]. Finger-mounted QME is particularly well-suited to these applications as the compact design is ideal for confined spaces such as a surgical cavity and the acquisition rate used (10 kHz) enables finger-mounted QME to be performed within several seconds, comparable to the time scale of some manual palpation techniques. Furthermore, OCT systems with acquisition times orders of magnitude faster than 10 kHz are readily available [53]. In this first demonstration of finger-mounted QME, we chose to use conservative acquisition times and to focus on the proof-of-principle. In future development, using faster acquisition times, combined with more rapid compression of the tissue with the finger, would allow measurements to be acquired in milliseconds.

The clinical suitability of finger-mounted QME could be enhanced by replacing the plastic thimble case with a surgical glove to ensure the probe can be used in sterile scenarios. Embedding the optical components in a glove would better preserve tactile sensation and could provide surgeons with improved dexterity over the rigid plastic case currently used. However, even the addition of a second set of gloves has shown reductions in hand sensitivity during surgery [54] and the addition of the optical fiber and associated components would more than likely incur a similar or greater reduction in sensitivity. As manual palpation is predominantly performed using the fingertips [3], positioning any components that would hinder sensitivity away from the fingertip would better preserve tactile sensitivity whilst still providing the surgeon with the benefits of QME.

5. Conclusions

This paper presented the first finger-mounted OCE probe. The probe features a forward-facing fiber probe in a compact implementation of QME. Demonstrations in 1D on silicone samples have shown that finger-mounted QME is capable of estimating the elasticity of materials within 21% of the expected value. Finger-mounted QME was also capable of measuring the thermally-induced changes in kangaroo muscle tissue. In addition, a preliminary 2D scan over an inclusion phantom showed the capability to detect features based on the mechanical contrast, albeit, at a reduced accuracy compared to the 1D measurements. With further enhancement of 2D scanning, we believe that finger-mounted QME has potential to augment existing clinical practices that rely on manual palpation.

Funding

Australian Research Council (ARC); the Cancer Council, Western Australia; OncoRes Medical; War Widows' Guild of Western Australia Scholarship.

Disclosures

BFK: OncoRes Medical (F, I) and AC, LC: OncoRes Medical (I). The other authors declare that there are no conflicts of interest related to this article.

References

1. R. H. Wilkins, "Neurosurgical Classic—XVII," J. Neurosurg. **21**, 240–244 (1964).
2. J. K. Harness, A. E. Giuliano, B. A. Pockaj, and E. Downs-Kelly, "Margins: a status report from the Annual Meeting of the American Society of Breast Surgeons," Ann. Surg. Oncol. **21**(10), 3192–3197 (2014).
3. D. Field and J. S. O. Hutchinson, *Field's Anatomy, Palpation, and Surface Markings* (Elsevier Health Sciences, 2006).
4. R. G. Pleijhuis, M. Graafland, J. de Vries, J. Bart, J. S. de Jong, and G. M. van Dam, "Obtaining adequate surgical margins in breast-conserving therapy for patients with early-stage breast cancer: current modalities and future directions," Ann. Surg. Oncol. **16**(10), 2717–2730 (2009).
5. K. J. Parker, M. M. Doyley, and D. J. Rubens, "Imaging the elastic properties of tissue: the 20 year perspective," Phys. Med. Biol. **56**(1), R1–R29 (2011).
6. J. Ophir, I. Céspedes, H. Ponnekanti, Y. Yazdi, and X. Li, "Elastography: a quantitative method for imaging the elasticity of biological tissues," Ultrason. Imaging **13**(2), 111–134 (1991).
7. A. P. Sarvazyan, O. V. Rudenko, S. D. Swanson, J. B. Fowlkes, and S. Y. Emelianov, "Shear wave elasticity imaging: a new ultrasonic technology of medical diagnostics," Ultrasound Med. Biol. **24**(9), 1419–1435 (1998).

Biomedical Optics EXPRESS

8. R. Muthupillai, D. J. Lomas, P. J. Rossman, J. F. Greenleaf, A. Manduca, and R. L. Ehman, "Magnetic resonance elastography by direct visualization of propagating acoustic strain waves," Science **269**(5232), 1854–1857 (1995).
9. L. Castera, X. Forns, and A. Alberti, "Non-invasive evaluation of liver fibrosis using transient elastography," J. Hepatol. **48**(5), 835–847 (2008).
10. M. Yin, J. A. Talwalkar, K. J. Glaser, A. Manduca, R. C. Grimm, P. J. Rossman, J. L. Fidler, and R. L. Ehman, "Assessment of hepatic fibrosis with magnetic resonance elastography," Clin. Gastroenterol. Hepatol. **5**(10), 1207–1213 (2007).
11. A. Evans, P. Whelehan, K. Thomson, D. McLean, K. Brauer, C. Purdie, L. Jordan, L. Baker, and A. Thompson, "Quantitative shear wave ultrasound elastography: initial experience in solid breast masses," Breast Cancer Res. **12**(6), R104 (2010).
12. B. F. Kennedy, P. Wijesinghe, and D. D. Sampson, "The emergence of optical elastography in biomedicine," Nat. Photonics **11**(4), 215–221 (2017).
13. R. K. Wang, S. Kirkpatrick, and M. Hinds, "Phase-sensitive optical coherence elastography for mapping tissue microstrains in real time," Appl. Phys. Lett. **90**(16), 164105 (2007).
14. A. Nahas, M. Bauer, S. Roux, and A. C. Boccara, "3D static elastography at the micrometer scale using Full Field OCT," Biomed. Opt. Express **4**(10), 2138–2149 (2013).
15. S. Wang and K. V. Larin, "Shear wave imaging optical coherence tomography (SWI-OCT) for ocular tissue biomechanics," Opt. Lett. **39**(1), 41–44 (2014).
16. J. A. Mulligan, G. R. Untracht, S. N. Chandrasekaran, C. N. Brown, and S. G. Adie, "Emerging approaches for high-resolution imaging of tissue biomechanics with optical coherence elastography," IEEE J. Sel. Top. Quant. **22**(3), 246–265 (2016).
17. V. Y. Zaitsev, L. A. Matveev, A. L. Matveyev, G. V. Gelikonov, and V. M. Gelikonov, "Elastographic mapping in optical coherence tomography using an unconventional approach based on correlation stability," J. Biomed. Opt. **19**(2), 021107 (2013).
18. S. Wang and K. V. Larin, "Optical coherence elastography for tissue characterization: a review," J. Biophotonics **8**(4), 279–302 (2015).
19. M. A. Kirby, I. Pelivanov, S. Song, Ł. Ambrozinski, S. J. Yoon, L. Gao, D. Li, T. T. Shen, R. K. Wang, and M. O'Donnell, "Optical coherence elastography in ophthalmology," J. Biomed. Opt. **22**(12), 1–28 (2017).
20. S. Wang, M. Singh, T. T. Tran, J. Leach, S. R. Aglyamov, I. V. Larina, J. F. Martin, and K. V. Larin, "Biomechanical assessment of myocardial infarction using optical coherence elastography," Biomed. Opt. Express **9**(2), 728–742 (2018).
21. B. F. Kennedy, R. A. McLaughlin, K. M. Kennedy, L. Chin, P. Wijesinghe, A. Curatolo, A. Tien, M. Ronald, B. Latham, C. M. Saunders, and D. D. Sampson, "Investigation of optical coherence microelastography as a method to visualize cancers in human breast tissue," Cancer Res. **75**(16), 3236–3245 (2015).
22. C. Li, G. Guan, Y. Ling, Y.-T. Hsu, S. Song, J. T.-J. Huang, S. Lang, R. K. Wang, Z. Huang, and G. Nabi, "Detection and characterisation of biopsy tissue using quantitative optical coherence elastography (OCE) in men with suspected prostate cancer," Cancer Lett. **357**(1), 121–128 (2015).
23. K. M. Kennedy, B. F. Kennedy, R. A. McLaughlin, and D. D. Sampson, "Needle optical coherence elastography for tissue boundary detection," Opt. Lett. **37**(12), 2310–2312 (2012).
24. G. van Soest, F. Mastik, N. de Jong, and A. F. W. van der Steen, "Robust intravascular optical coherence elastography by line correlations," Phys. Med. Biol. **52**(9), 2445–2458 (2007).
25. Q. Fang, A. Curatolo, P. Wijesinghe, Y. L. Yeow, J. Hamzah, P. B. Noble, K. Karnowski, D. D. Sampson, R. Ganss, J. K. Kim, W. M. Lee, and B. F. Kennedy, "Ultrahigh-resolution optical coherence elastography through a micro-endoscope: towards in vivo imaging of cellular-scale mechanics," Biomed. Opt. Express **8**(11), 5127–5138 (2017).
26. K. M. Kennedy, C. Ford, B. F. Kennedy, M. B. Bush, and D. D. Sampson, "Analysis of mechanical contrast in optical coherence elastography," J. Biomed. Opt. **18**(12), 121508 (2013).
27. X. Liu, F. Zaki, and Y. Wang, "Quantitative optical coherence elastography for robust stiffness assessment," Appl. Sci. (Basel) **8**(8), 1255 (2018).
28. A. A. Sovetsky, A. L. Matveyev, L. A. Matveev, D. V. Shabanov, and V. Y. Zaitsev, "Manually-operated compressional optical coherence elastography with effective aperiodic averaging: demonstrations for corneal and cartilaginous tissues," Laser Phys. Lett. **15**(8), 085602 (2018).
29. K. M. Kennedy, L. Chin, R. A. McLaughlin, B. Latham, C. M. Saunders, D. D. Sampson, and B. F. Kennedy, "Quantitative micro-elastography: imaging of tissue elasticity using compression optical coherence elastography," Sci. Rep. **5**(1), 15538 (2015).
30. W. M. Allen, K. M. Kennedy, Q. Fang, L. Chin, A. Curatolo, L. Watts, R. Zilkens, S. L. Chin, B. F. Dessauvagie, B. Latham, C. M. Saunders, and B. F. Kennedy, "Wide-field quantitative micro-elastography of human breast tissue," Biomed. Opt. Express **9**(3), 1082–1096 (2018).
31. G. Lamouche, B. F. Kennedy, K. M. Kennedy, C.-E. Bisaillon, A. Curatolo, G. Campbell, V. Pazos, and D. D. Sampson, "Review of tissue simulating phantoms with controllable optical, mechanical and structural properties for use in optical coherence tomography," Biomed. Opt. Express **3**(6), 1381–1398 (2012).
32. K. M. Kennedy, S. Es'haghian, L. Chin, R. A. McLaughlin, D. D. Sampson, and B. F. Kennedy, "Optical palpation: optical coherence tomography-based tactile imaging using a compliant sensor," Opt. Lett. **39**(10), 3014–3017 (2014).

Biomedical Optics EXPRESS

33. B. F. Kennedy, S. H. Koh, R. A. McLaughlin, K. M. Kennedy, P. R. T. Munro, and D. D. Sampson, "Strain estimation in phase-sensitive optical coherence elastography," Biomed. Opt. Express **3**(8), 1865–1879 (2012).
34. S. J. Kirkpatrick, R. K. Wang, and D. D. Duncan, "OCT-based elastography for large and small deformations," Opt. Express **14**(24), 11585–11597 (2006).
35. E. Tornberg, "Effects of heat on meat proteins - Implications on structure and quality of meat products," Meat Sci. **70**(3), 493–508 (2005).
36. G. J. Lewis and P. P. Purslow, "The strength and stiffness of perimysial connective tissue isolated from cooked beef muscle," Meat Sci. **26**(4), 255–269 (1989).
37. K. Li, R. Nataraj, T. L. Marquardt, and Z.-M. Li, "Directional coordination of thumb and finger forces during precision pinch," PLoS One **8**(11), e79400 (2013).
38. P. Wijesinghe, L. Chin, and B. F. Kennedy, "Strain tensor imaging in compression optical coherence elastography," IEEE J. Sel. Top. Quant. **25**(1), (2019).
39. T. A. Krouskop, T. M. Wheeler, F. Kallel, B. S. Garra, and T. Hall, "Elastic moduli of breast and prostate tissues under compression," Ultrason. Imaging **20**(4), 260–274 (1998).
40. L. Castéra, J. Vergniol, J. Foucher, B. Le Bail, E. Chanteloup, M. Haaser, M. Darriet, P. Couzigou, and V. De Lédinghen, "Prospective comparison of transient elastography, Fibrotest, APRI, and liver biopsy for the assessment of fibrosis in chronic hepatitis C," Gastroenterology **128**(2), 343–350 (2005).
41. P. Wijesinghe, D. D. Sampson, and B. F. Kennedy, "Computational optical palpation: a finite-element approach to micro-scale tactile imaging using a compliant sensor," J. R. Soc. Interface **14**(128), 20160878 (2017).
42. C. D. Lu, M. F. Kraus, B. Potsaid, J. J. Liu, W. Choi, V. Jayaraman, A. E. Cable, J. Hornegger, J. S. Duker, and J. G. Fujimoto, "Handheld ultrahigh speed swept source optical coherence tomography instrument using a MEMS scanning mirror," Biomed. Opt. Express **5**(1), 293–311 (2014).
43. K. H. Kim, B. H. Park, G. N. Maguluri, T. W. Lee, F. J. Rogomentich, M. G. Bancu, B. E. Bouma, J. F. de Boer, and J. J. Bernstein, "Two-axis magnetically-driven MEMS scanning catheter for endoscopic high-speed optical coherence tomography," Opt. Express **15**(26), 18130–18140 (2007).
44. P. H. Tran, D. S. Mukai, M. Brenner, and Z. Chen, "In vivo endoscopic optical coherence tomography by use of a rotational microelectromechanical system probe," Opt. Lett. **29**(11), 1236–1238 (2004).
45. Y. Pan, H. Xie, and G. K. Fedder, "Endoscopic optical coherence tomography based on a microelectromechanical mirror," Opt. Lett. **26**(24), 1966–1968 (2001).
46. B. Y. Yeo, R. A. McLaughlin, R. W. Kirk, and D. D. Sampson, "Enabling freehand lateral scanning of optical coherence tomography needle probes with a magnetic tracking system," Biomed. Opt. Express **3**(7), 1565–1578 (2012).
47. N. Uribe-Patarroyo and B. E. Bouma, "Rotational distortion correction in endoscopic optical coherence tomography based on speckle decorrelation," Opt. Lett. **40**(23), 5518–5521 (2015).
48. C. E. DeSantis, C. C. Lin, A. B. Mariotto, R. L. Siegel, K. D. Stein, J. L. Kramer, R. Alteri, A. S. Robbins, and A. Jemal, "Cancer treatment and survivorship statistics, 2014," CA Cancer J. Clin. **64**(4), 252–271 (2014).
49. S. E. Singletary, "Surgical margins in patients with early-stage breast cancer treated with breast conservation therapy," Am. J. Surg. **184**(5), 383–393 (2002).
50. H. Ballal, D. B. Taylor, A. G. Bourke, B. Latham, and C. M. Saunders, "Predictors of re-excision in wire-guided wide local excision for early breast cancer: a Western Australian multi-centre experience," ANZ J. Surg. **85**(7-8), 540–545 (2015).
51. J. A. Knol, C. S. Marn, I. R. Francis, J. M. Rubin, J. Bromberg, and A. E. Chang, "Comparisons of dynamic infusion and delayed computed tomography, intraoperative ultrasound, and palpation in the diagnosis of liver metastases," Am. J. Surg. **165**(1), 81–87 (1993).
52. T. C. Böttger, W. Weber, J. Beyer, and T. Junginger, "Value of tumor localization in patients with insulinoma," World J. Surg. **14**(1), 107–112 (1990).
53. W. Wieser, B. R. Biedermann, T. Klein, C. M. Eigenwillig, and R. Huber, "Multi-Megahertz OCT: high quality 3D imaging at 20 million A-scans and 4.5 GVoxels per second," Opt. Express **18**(14), 14685–14704 (2010).
54. S. J. Wilson, D. Sellu, A. Uy, and M. A. Jaffer, "Subjective effects of double gloves on surgical performance," Ann. R. Coll. Surg. Engl. **78**(1), 20–22 (1996).